ADVANCED FUNCTIONAL MATERIALS
www.afm-journal.de

Tunable Ferroelectric Topological Defects on 2D Topological Surfaces: Complex Strain Engineering Skyrmion-Like Polar Structures in 2D Materials

Bo Xu, Zhanpeng Gong, Jingran Liu, Yunfei Hong, Yang Yang, Lou Li, Yilun Liu, Junkai Deng, and Jefferson Zhe Liu**

Polar topological structures in ferroelectric materials have attracted significant interest due to their fascinating physical properties and promising applications in high-density, nonvolatile memories. Currently, most polar topological patterns are only observed in the bulky perovskite superlattices. In this work, a discovery of tunable ferroelectric polar topological structures is reported, designed, and achieved using topological strain engineering in two-dimensional (2D) PbX (X = S, Se, and Te) materials via integrating first-principles calculations, machine learning molecular dynamics simulations, and continuum modeling. First-principles calculations discover the strain-induced reversible ferroelectric phase transition with diverse polarization directions strongly correlated to the straining conditions. Taking advantage of the mechanical flexibility of 2D PbX, using molecular dynamics (MD) simulations, it is successfully demonstrated that the complex strain fields of 2D topological surfaces under mechanical indentation can generate unique skyrmion-like polar topological vortex patterns. Further continuum simulations for experimentally accessible larger-scale 2D topological surfaces uncover multiple skyrmion-like structures (i.e., vortex, anti-vortex, and flux-closure) and transition between them by adopting/designing different types of mechanical loadings (such as out-of-plane indention and air blowing). Topological surfaces with various designable reversible polar topological structures can be tailored by complex straining flexible 2D materials, which provides excellent opportunities for next-generation nanoelectronics and sensor devices.

1. Introduction

Topological objects with vortical configuration, such as skyrmion,[1] meron,[2,3] and other toroidal topological states,[4–6] come on stage with intriguing properties in potential nonvolatile memory. Distinguished from the magnetic skyrmion of quasiparticles, the electric-polar topological structures with various vortex and polar skyrmion have been observed in recent years and developed promising functionalities of these topological structures.[7–9] For example, the array of flux-closure quadrants was first discovered in strained ferroelectric (FE) $PbTiO_3$ films.[10] Various topological states, including polar skyrmion, were then reported in the superlattices of $PbTiO_3/SrTiO_3$.[5,6,8] These unique structures gave birth to exciting features like the negative-capacitance effect, ultrafast collective dynamics at the terahertz level, and promising high-density non-volatile memory.[11–14]

These skyrmion-like topological structures originate from the interaction between inherent strain, depolarization field, and charges through the strategy of heterointerface and epitaxial strains. So far, the polar topological patterns have been mostly observed in the thin films and bulk bubble domains of perovskite superlattices, e.g., $(PbTiO_3)_n/(SrTiO_3)_n$ superlattice[15,16] and bubble domains of bulk $Bi_{0.5}Na_{0.5}TiO_3$.[17,18] The thickness of these widely investigated perovskite oxides materials are mostly more than ten unit-cells, e.g., the $(SrTiO_3)_n/(PbTiO_3)_n/(SrTiO_3)_n$ ($n \geqslant 12$) trilayered superlattices,[19] the $[(PbTiO_3)_{16}/(SrTiO_3)_{16}]_8$ superlattice membrane[20] and the $PbTiO_3$ thin film with thickness of

B. Xu, Z. Gong, Y. Hong, Y. Yang, L. Li, J. Deng
State Key Laboratory for Mechanical Behavior of Materials
School of Materials Science and Engineering
Xi'an Jiaotong University
Xi'an 710049, China
E-mail: junkai.deng@mail.xjtu.edu.cn

The ORCID identification number(s) for the author(s) of this article can be found under https://doi.org/10.1002/adfm.202311599

DOI: 10.1002/adfm.202311599

J. Liu, Y. Liu
State Key Laboratory for Strength and Vibration of Mechanical Structures
School of Aerospace Engineering
Xi'an Jiaotong University
Xi'an 710049, China

J. Z. Liu
Department of Mechanical Engineering
The University of Melbourne
Parkville VIC 3010, Australia
E-mail: zhe.liu@unimelb.edu.au

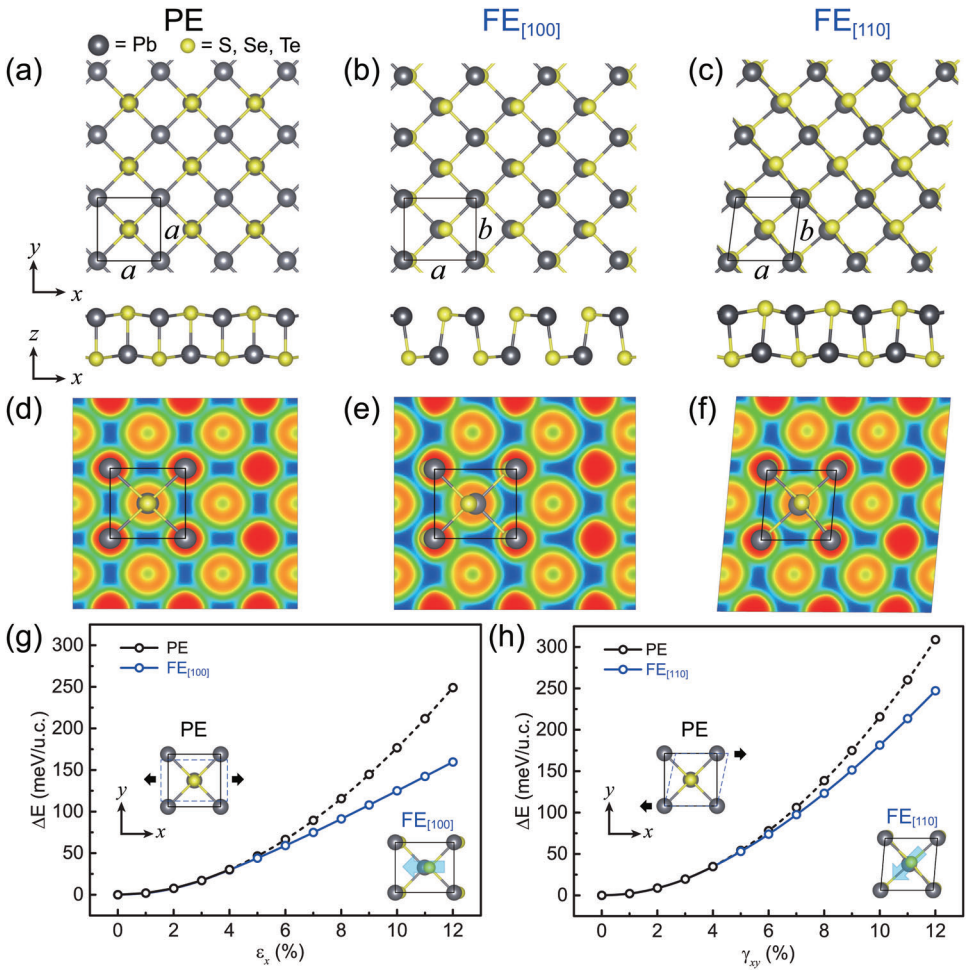

Figure 1. The PE, $FE_{[100]}$, and $FE_{[110]}$ phases for monolayer PbX and the total energy variation under mechanical loadings. a). The atomic structures of the PE, $FE_{[100]}$, and $FE_{[110]}$ phases for monolayer PbX. d–f) The corresponding electron localization function (ELF) for the three phases. There are five, three, and four atomic bonds for each chalcogenide atom in PE, $FE_{[100]}$, and $FE_{[110]}$ phases, respectively. g,h) The energy variation of monolayer PbTe under uniaxial stretch and in-plane shear. The parabolic energy curve turns into a smoother curve when the applied stretch and shear strain is beyond 3.5% and 3.6%, respectively.

5–13 nm.[21] Over the years, two-dimensional (2D) FE materials have attracted significant interest. The 2D FE materials exhibit intrinsic nanoscale thickness (even with just one unit-cell thickness), tunable polarization, excellent mechanical flexibility, and superior mechanical strength. They can be used in highly integrated and miniaturized electronic elements,[22–24] as well as flexible nanoelectronics.[25–27] Notably, the excellent mechanical deformability and flexibility endow 2D FE materials with the ability to sustain large and complex strain fields under some designed mechanical loadings.[28,29] Various polarization assemblies, including the desirable topological polar structures, could be produced under such complex strain fields.[30]

In this work, we report the discovery of tunable 2D topological defective structures of ferroelectric polarization, designed in the 2D topological surfaces of lead monochalcogenides materials (PbX, X = S, Se, and Te). The strain-induced paraelectric (PE) to FE transition in 2D PbX is demonstrated by density functional theory (DFT) first-principles calculations. Then, with the developed deep-learning potential, our large-scale molecular dynamics (MD) simulations reveal that mechanical indentation introduces a complex inhomogeneous strain field to a 2D PbX topological surface and thus generates a skyrmion-like flux-closure polar topological pattern. To demonstrate the universality of this concept at larger scales that are experimentally accessible, three unique regimes of inhomogeneous strain fields are sequentially proposed through strain engineering in such 2D materials. Our finite element method (FEM) simulations demonstrate multiple skyrmion-like polar topological patterns, i.e., vortex, anti-vortex, and flux-closure, on the mechanically formed topological surfaces of 2D PbX under different mechanical loads. The strategy to induce topological polar states by complex strain field engineering broadens the way for the potential application of topological polar patterns.

2. Results and Discussion

Group-IV monochalcogenides (e.g., GeS, GeSe, SnS, SnSe) are a group of newly discovered FE materials whose broken

centrosymmetric and puckered structures endow them with large electric polarization.[31,32] Monolayer PbX (X = S, Se, and Se) has in-plane fourfold symmetry with a lattice constant a = 4.237, 4.400, and 4.638 Å for PbS, PbSe, and PbTe, respectively. Unlike other group-IV monochalcogenides with a noncentrosymmetric puckered structure (space group *Pnma*), the ground state of PbX (**Figure 1a**) shows a high symmetric non-polarized paraelectric (PE) structure, in which the Pb and X atoms align in the *z*-direction (space group *Cmcm*). The phonon spectrum also demonstrates the structural stability of this PE structure even down to 0 K. The experimental STM topography images demonstrate that the thickness of monolayer PbTe is even less than 1.5 nm.[33]

Herein, two kinds of strains were applied to generate long-range ferroelectric order in monolayer PbX. Figure 1g shows the total energy variation of monolayer PbTe under a uniaxial strain along the *x* direction. The total energy keeps parabolically increasing till a critical strain and then follows another parabolic curve, indicating a phase transition. At a critical value of 3.5%, a new phase of PbTe can be observed, showing a black phosphorene-like puckered structure with ferroelectric polarization along the *x* direction. We named it the $FE_{[100]}$ phase (Figure 1b). In addition, an in-plane shear strain is applied to the pristine PE phase (Figure 1h). With the applied shear strain increased to a critical value of 4.0%, a FE transition occurs but in the diagonal direction of *x*-*y* plane. We named it the $FE_{[110]}$ phase (Figure 1c). The contour maps of electron localization function (ELF) for the three phases illustrate their covalent bonding structures are different, i.e., each Te atom shares 5, 3, and 4 covalent bonds with surrounding Pb atoms in PE, $FE_{[100]}$, and $FE_{[110]}$, respectively (Figure 1d–f), corresponding to a phase with non-polarized, polarized in *x* direction, and polarized in diagonal direction. Similar ferroelectric phase transitions also happened in monolayer PbS and PbSe (Figure S1, Supporting Information). The values of critical strain are summarized in **Table 1**.

Table 1. The lattice parameters and phase transition strain for monolayer PbX.

Materials	*a*(Å)	$\varepsilon_x/\varepsilon_y$	γ_{xy}
PbS	4.237	1.6%	2.1%
PbSe	4.400	2.2%	2.4%
PbTe	4.638	3.5%	3.6%

Taking the uniaxial stretch of PbTe as an example, the projected distance of Pb and Te atoms in the *x*-*y* plane (d_{Pb-Te}) is taken as the order parameter. Figure S2a (Supporting Information) shows the relative total energy (ΔE) as a function of the order parameter. When the applied tensile strain is lower than the critical strain (3.5% for PbTe), the total energy curve is parabolic increasing, and the state with zero order parameter (FE state) is the ground state. When the applied tensile strain is higher than the critical strain, two bistable FE states with non-zero order parameters arise, corresponding to the two equivalent states with non-zero polarization along the [$\bar{1}$00] and [100] directions, respectively. The total energy curve and its derivative with respect to the strain (Figure S3, Supporting Information) imply the feature of continuous phase transition. In analogy with the phase transition in traditional FE perovskite materials, increasing external strain can lead to the PE-to-FE phase transition in 2D FE PbX materials.

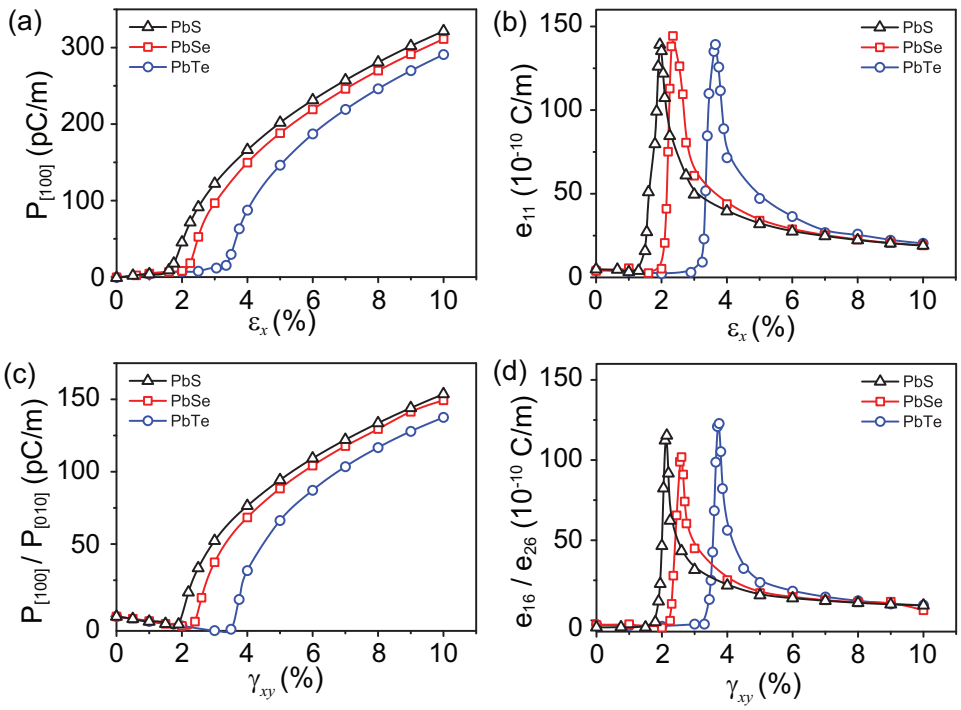

Figure 2. The ferroelectric polarization and corresponding piezoelectric coefficient as a function of applied strain. a) The FE polarization changes under uniaxial strain. b) The piezoelectric coefficient e_{11} changes under uniaxial strain. c) The FE polarization changes along [100]/[010] direction under shear strain. d) The piezoelectric coefficient e_{16}/e_{26} changes under shear strain.

Table 2. The piezoelectric coefficients for monolayer PbX under mechanical loadings.

Materials	Stretch		Shear	
	Max e_{11}	Final e_{11}	Max e_{16}	Final e_{16}
PbS	139.1	19.0	115.3	9.3
PbSe	144.3	19.1	101.9	6.3
PbTe	139.2	20.4	122.8	9.4
			Unit: 10^{-10}C m^{-1}	

The stability of strained structures is also examined by phonon dispersion calculations (Figures S3–S5, Supporting Information). For PbTe monolayer, the phonon dispersion spectra of the ground state (i.e., PE) show no negative frequency, indicating its dynamic stability (Figure S2b, Supporting Information). With the tensile strain increasing, the frequency of phonons gradually softens. Particularly, a negative frequency (i.e., soft optical mode) at the gamma point rises when the applied strain is close to the critical point. The soft optical modes related to displacive instabilities have been assigned to be the origin of spontaneous symmetry breaking in the ferroelectric phase transition. Further analysis reveals that this soft vibration mode corresponds to the Te atom moving away from the Pb atoms in the x direction, which leads to the breaking of the centrosymmetry with polarization in the [100] direction (Figure S2c, Supporting Information). As a result, symmetry breaking leads to the phase transition from PE to FE phase. Similar phonon dispersion results are also obtained during the shear strain process, revealing the occurrence of spontaneous polarization in the [110] direction above critical shear strain. Previous experimental and theoretical works also investigated the physical origin of the ferroelectric instability of bulk PbTe, and support the interpretation about the strain induced paraelectric-to-ferroelectric phase transition in our 2D PbTe materials.[34–36]

Figure 2 shows the polarization change with increasing external strain. The Berry phase theory is employed to determine the polarization values.[37,38] The corresponding polarization with respect to the tensile strain and shear strain are shown in Figure 2a,c, respectively. The phase transition accompanies an abrupt polarization change from zero to a non-zero value at the critical strain, beyond which the polarization continually increases. Figure 2b,d summarize the piezoelectric coefficient, defined as the derivative of polarization with respect to strain. We observe an enormous piezoelectric burst of e_{11} (139.1, 144.3, and 139.2×10^{-10} C m^{-1} for PbS, PbSe, and PbTe, respectively[39]) accompanying the phase transition and then a gradual convergence to a stable piezoelectric coefficient e_{11} about 2×10^{-9} C m^{-1}. The convergent piezoelectric coefficients are comparable with other group-IV monochalcogenides, such as SnS and SnSe (1.81 and 3.49×10^{-9} C m^{-1}, respectively). The maximum and converged e_{11} values are summarized in **Table 2**. As for the case of shear deformation, a similar tendency can be observed. Table 2 summarizes the piezoelectric coefficient results. The enormous piezoelectric effects could enable promising applications in nanoscale sensors and energy harvesting devices.

The strain states of 2D materials under loading are usually rather complex in experiments.[28,40] We also investigate the PE-to-FE transition under the planar strain conditions, i.e., normal strain along the x and y directions and the in-plane shear strain. The normal strain ranging from −7% to 7% in both x and y directions and/or shear strain ranging from 0 to 8% is applied to the pristine PE PbX. **Figure 3a** shows the polarization-strain diagram of PbTe, including a set of contour plots at some given shear strain values. In one contour plot, the color map depicts the polarization magnitude at a given shear strain value. The grey areas represent the PE phase with zero polarization. The clear phase boundary represents the critical strain values. Increasing the applied shear strain values expands the FE phase region, i.e., reducing the critical normal strain values for the PE-to-FE transition.

Figure 3b shows the FE polarization directions. When only normal strain is applied, the polarization of the ferroelectric phase is along the x direction when $\varepsilon_x > \varepsilon_y$, and vice versa. This is consistent with the rectangular shape of the deformed unit cell. For the case of equal biaxial strain $\varepsilon_x = \varepsilon_y$, the FE polarization is along the diagonal direction [110]. There is a sharp polarization direction change in the diagonal axis of the polarization direction-strain diagram. We notice that the shear strain plays a significant and interesting role in the change of polarization direction. Generally, under a certain shear strain: $\gamma_{xy} = 0.02$, 0.04, and 0.06, the polarization direction rotates to fall in between [100]/[010] and [110] directions. Intuitively, a shear strain changes the [100] and [010] crystal direction toward the diagonal axis and thus rotates the polarization directions of the zero-shear strain case (first plot in Figure 3b) accordingly. But a close inspection reveals that the FE directions do not rotate conformably with the crystalline directions. This indicates the existence of some FE states other than the observed $FE_{[100]}$/ $FE_{[010]}$, and $FE_{[110]}$ phases (Figure 1). The apparent continuous FE direction rotation in Figure 3b suggests the continuously distributed stable FE states between the $FE_{[100]}$ and $FE_{[110]}$ states under the planar strain conditions, which is distinctive from the conventional FE materials. This new feature could be attributed to the covalent bonding nature of the PbX materials. Note that similar impressive works reported 2D ferroelectric PbTe under tension.[41,42] In the present work, all possible in-plane strains are considered, i.e., bi-axial tensile and compressive strain and in-plane shear strain. The relation between in-plane strain and polarization is then comprehensively studied here.

Deforming atomically thin 2D materials to topological surfaces can generate complicated strain fields. In turn, it is possible to generate interesting FE topological structures based on the polarization-strain diagram, which are not observed in bulk conventional FE ceramic materials. To examine this hypothesis, we developed a deep-learning potential to perform molecular dynamics (MD) simulations for the polarization distribution of a monolayer PbX under mechanical loading. The details of our deep-learning potential are provided in Methodology section. **Figure 4a** shows our molecular model where a spherical tip with a radius of 3.5 nm is employed to indent a suspended monolayer PbTe membrane with the size of 60 × 60 units (i.e., about 28 × 28 nm) at 300 K. At the indentation depth of 2.4 nm, the local strain value in the membrane center is beyond the critical phase transition point. An interesting vortical polarization pattern emerges on the topological cone/tent surface (Figure 4b), in which FE dipoles form a continuous clockwise loop in the central region. Four domains can be divided along the two diagonal lines. The net polarization of each domain largely aligns along either the x or y-axis. Near the domain boundaries,

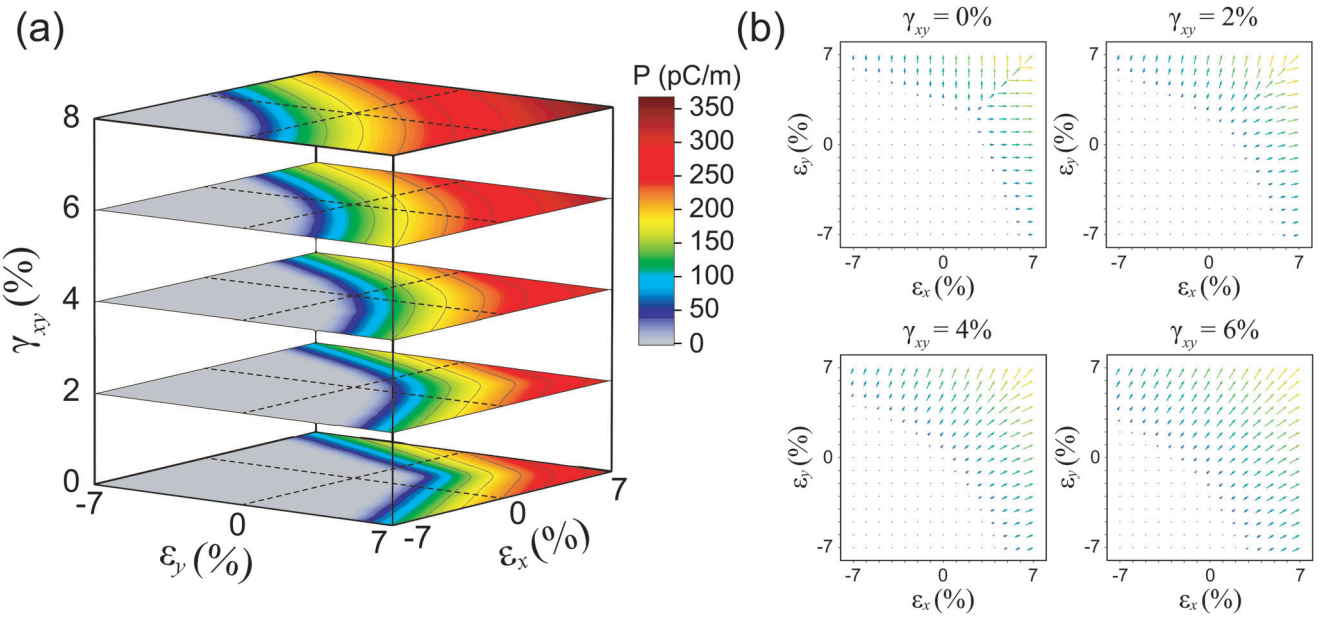

Figure 3. Polarization-strain diagram of monolayer PbTe. a) The whole diagram under the combined in-plane biaxial strain and shear strain. The boundary between grey and other colored area represents the phase boundary between PE and FE phases. b) The polarization map under in-plain biaxial strain combined with the shear strain of 0%, 2%, 4%, and 6%, respectively. The arrows represent the polarization values and directions at a specific strain condition.

the 45° dipoles can be observed. This is the first example of a vortical polarization pattern in a pristine 2D material.

Figure 4c–e shows the inhomogeneous strain field in center area (20 × 20 units) and Figure S7 (Supporting Information) shows the whole maps of 60 × 60 units. The distortion of one unit cell is divided into three components, ε_x and ε_x, and γ_{xy}. The strain value gradually reduces from the centre area to the fixed boundary regions. Based on the MD strain distribution field, using the polarization-strain diagram (Figure 3), we generate the polarization map (Figure S8, Supporting Information). This map agrees very well with the polarization map determined by direct MD simulations. In other words, the local strain distributions are closely related to the polarization distribution. This indicates that the local strain is the primary driving force for generating the vortical FE topological defects rather than other forces such as dipole-dipole Coulombic interaction.

Such a strong correlation between polarization and strain motivates us to employ the FEM simulation to determine the complex strain fields on different topological surfaces of a PbX monolayer and thus the resultant topological polar defective patterns. We examined three geometric models and two different types of loads, as shown in **Figure 5**. The geometry is similar to Figure 4, i.e., a 2D monolayer membrane deposited on a substrate with a hole of a certain shape (round or square). The boundary is clamped. A mechanical load is applied via either a spherical tip (radius from 3.5 nm to 11.5 nm) or a uniform pressure (to mimic gas blow). The constitutive relationship of the PE and FE phase are obtained based on DFT calculations, which are summarized in the Table S1 (Supporting Information). Note that the elastic constant, C_{11}, of the FE phase is only 6.228 N m^{-1}, much less than that of the PE phase (i.e., 38.064 N m^{-1}), indicating the softness along the armchair direction. In our FEM simulations, we considered the phase transition and the different mechanical properties of the FE and PE phases during loading. The strain criterion is implemented on the fly, i.e., when the local strain falls in the PE or FE phase regime (Figure 3), the elastic parameters of the PE or FE phase are employed. To verify the FEM model, we compared the results of the same model from MD simulation and FEM simulation. The flux-closure like polarization pattern from FEM is shown in Figure S9 (Supporting Information). The pattern and strain fields match very well with the polarization pattern obtained in MD simulation.

Figure 5a shows the three geometric models. The first model has a square hole with an edge length of 25 nm with PbX crystal direction aligned along the edges (termed as square-hole-0° model). The second model has a round hole with a diameter of 25 nm (named as round-hole model). The third model has a square hole with an edge length of 18 nm, on top of which one PbX monolayer rotated 45° relative to the edges is placed (termed as square-hole-45° model). Note that the diagonal direction length of the third geometric model is ≈25 nm, consistent with the other two cases.

The first type of mechanical load is applied via a spherical tip with a diameter from 3.5 to 11.5 nm in the middle of the membrane. It corresponds to a concentrated force. This is to mimic the experiment situations. For example, a diamond atomic force microscopy (AFM) tip was used to apply mechanical loading on suspended graphene to measure its mechanical strength. A graphene nano-tent was formed by placing graphene over a long sharp needle nanofabricated on a Si substrate.[40,43,44] Figure 5b shows the FE topological polarization pattern of above three geometric models indented by a tip of 3.5 nm from our FEM simulation. At an indentation depth of 1.2 nm, a vortex polarization pattern emerges. Interestingly, if we indent the

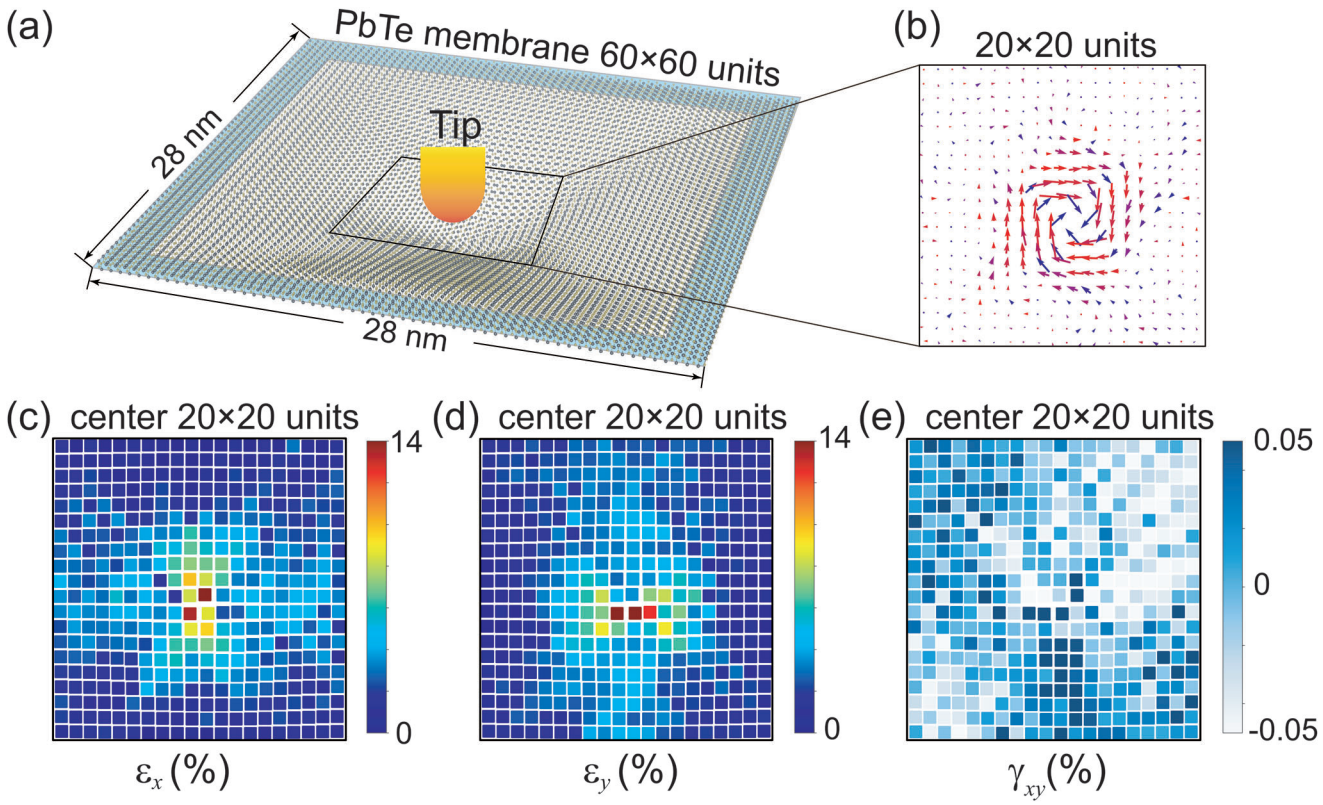

Figure 4. Topological polarization defects of monolayer PbTe under mechanical indentation. a) The schematic of mechanical indentation of monolayer PbTe (60 × 60 units) by a tip. b) The polar vortex structure was observed at the center of monolayer PbTe. Each arrow represents the net polarization of a unit-cell. c–e) The distribution of three components of lattice distortion at the center of monolayer PbTe (20 × 20 units). Each block unit represents the local lattice strain of a unit-cell, including the relative change of lattice parameters a and b, and the shear distortion of the unit-cell in the local tangent plane. The distribution of lattice distortion of the whole 60 × 60 units can be found in Figure S7 (Supporting Information). It demonstrates that the possible polarization pattern is closely dependent on the inhomogeneous strain distribution.

membrane up to a depth of 2.4 nm, the pattern grows and evolves to a distinct anti-vortex pattern. When a tip with larger radius is used, the initial patterns gradually become more disordered. But the final patterns always keep anti-vortex structures. The calculated strain fields and corresponding polarization maps are demonstrated in Figures S9– S20 (Supporting Information). The evolutions of polarization under different tip size and indent depth are demonstrated in Figures S21– S23 (Supporting Information).

In experiments, a uniform pressure could be applied on a 2D membrane via gas blowing.[28] We examined this second type of mechanical load using FEM simulations. Here, the PbTe membrane size is increased to 100 nm to be consistent with the experimental setup. Figure 5c shows the polarization map of the center (60 × 60 nm) of the membrane. The strain distribution is more homogeneous under this uniform pressure (Figure S24, Supporting Information). The round-hole and square-hole-0° models develop anti-vortex patterns, which are similar to the tip loading condition. However, the square-hole-45° model exhibits a flux-closure pattern instead, which is a similar structure observed in ferromagnetic materials and ferroelectric perovskite materials.[45–47] Loading conditions, therefore, can also be used to design desired topological polarization defects on 2D topological surfaces.

The quantitative results of tip indent loading cases are summarized in Figure 5d. For all three geometry models, a smaller tip size (3.5 and 7.5 nm) initially generates a vortex pattern, which eventually evolves into anti-vortex at a sufficiently large indent depth (beyond 2 nm). For a larger tip size (11.5 nm), a disordered pattern initially shows up, and it finally evolves into the anti-vortex pattern. The critical transition strain reduces with the increase of tip size. The square-hole-45° model has the smallest critical transition strains. Regarding the uniform pressure loading, Figure 5e shows model I and II always keep an anti-vortex pattern and model III keep a flux-closure pattern. It may attribute to the moderate strain change in each quadrant. Controlling the 2D material geometry, loading type, tip size, and indent depth are effective means for designing desirable skyrmion-like polarization topological defect on the generated 2D topological surfaces.[48,49]

Our predicted topological polar structures are diverse, depending on the shape of the hole, the membrane orientation, and the loading conditions. More complicated shapes, i.e., polygonal holes and sectorial holes, could be designed to enable more types of topological polar structures. Interestingly, vortex-oriented ferroelectric domains had been experimentally observed in the SnTe/PbTe monolayer lateral heterostructures.[33] This observation can be attributed to the mismatch strain and the

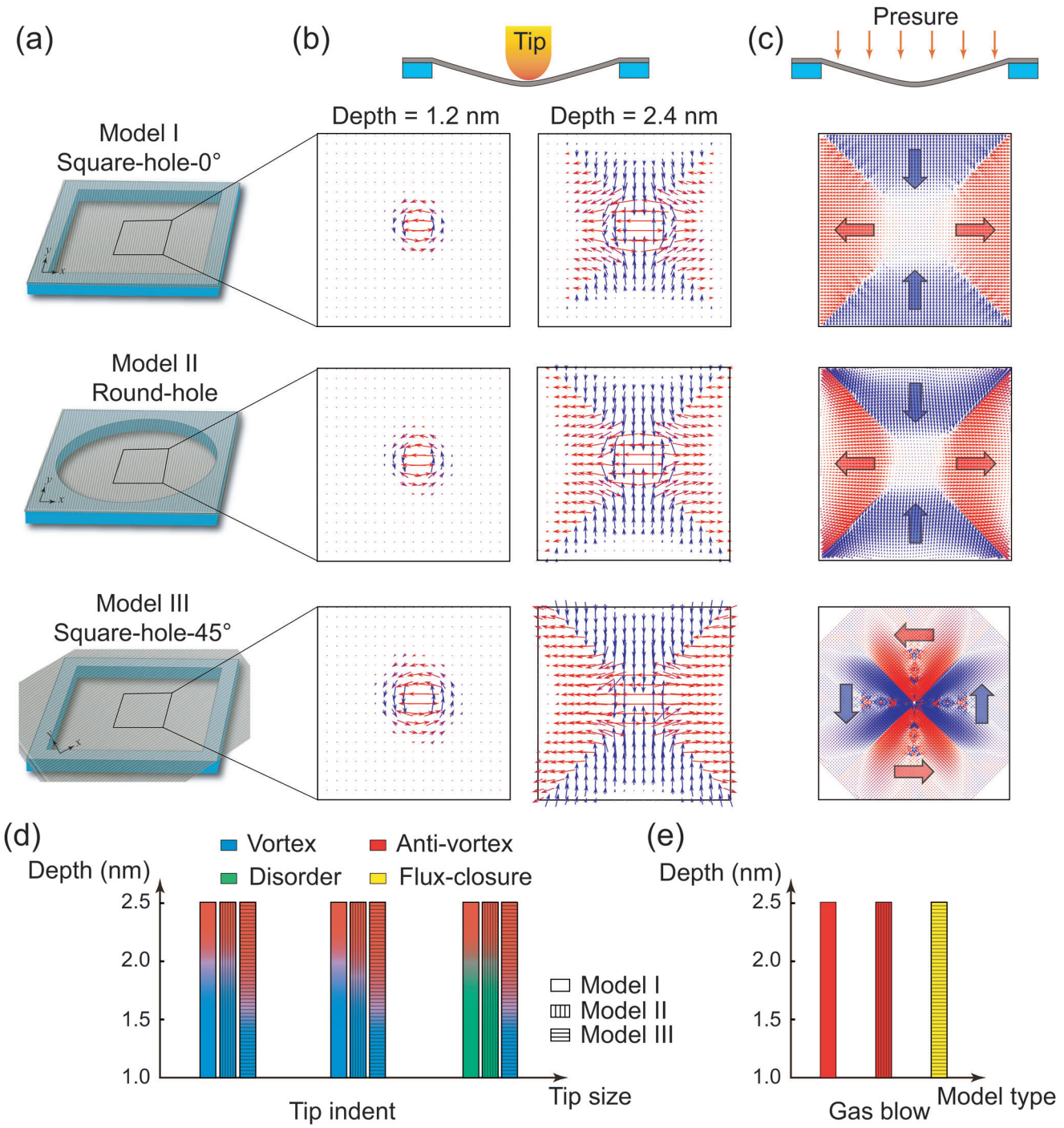

Figure 5. Topological polar structures of three designed models of the monolayer PbTe membrane. a) The geometry of the three models. Model I: monolayer PbTe membrane (28 × 28 nm) onto a substrate with a square hole (a = 25 nm). The direction of the lattice is arranged along the edge of hole. Model II: monolayer PbTe membrane onto a substrate with a circle hole (d = 25 nm). Model III: the monolayer PbTe rotates 45° based on model I (a = 18 nm). b) The vortex and anti-vortex patterns of polarization at indentation depth of 1.2 and 2.4 nm, under a tip radius of 3.5 nm. c) The anti-vortex and flux-closure patterns of polarization under uniform pressure loading of blowing bubble in the center of 100 × 100 nm of membrane. d,e) The summary of patterns under different loading, model, tip size and depth.

interfacial effects of the lateral heterostructures. It supports the conclusion of the present work, i.e., the strain-induced polar topological structures on flexible 2D materials. Moreover, as mentioned above, the present FE phase transition is reversible for monolayer PbX. Once the strain field is released, the FE phase turns back to the pristine PE phase. It suggests that the triggered topological defective patterns can be controllable and removable by external loadings.[50,51]

While the vortex structure induced by AFM tip loading in $BaTiO_3$ thin films has been reported by previous phase field simulation,[52] our research expands the scope of ferroelectric topological structures beyond the widely studied perovskite superlattices to 2D ferroelectric materials. Thanks to their mechanical flexibility, more complex strain conditions can be generated on 2D materials, such as nanoindentation, nanobubble, nanotent, scroll, fold, wrinkle, and conformable patterns,[28] far beyond the case demonstrated in perovskite materials. In this work, we illustrate the impact of inhomogeneous strain fields on the FE topological state in 2D PbTe materials using nanoindentation and nanobubble as two geometric topology examples.

In addition, alloying with other IV-VI materials could serve as a potential method to drive PbTe materials to the ferroelectric state.[53] It is also promising to design complex FE topological structures. Besides, unlike current 2D PbTe with an initial paraelectric phase, other intrinsic 2D FE materials, such as 2D β-PbTe with an original ferroelectric phase,[54] also hold great potential for applying complex strain loadings and corresponding deformations. It is thus reasonable to expect the various complicated topological polar structures achievable by strain engineering in other easy-deformable 2D FE materials. This opens a new avenue for creating novel ferroelectric physics and applications in 2D materials.

3. Conclusion

In this work, by integrating DFT calculation, MD simulations using deep-learning potential, and FEM simulation, we discover the strain-induced PE-to-FE phase transition and design the various skyrmion-like FE topological defects on 2D PbX topological surfaces. The underlying mechanism is the strong correlation between FE polarization and in-plane strain, as predicted in DFT calculations. By taking advantage of the mechanical robustness and flexibility of atomically thin 2D PbX, our MD and FEM simulations demonstrate that the complex strain fields generated on the 2D topological surfaces (under mechanical loading) can produce interesting and unexpected skyrmion-like FE topological defects, such as vortex, anti-vortex, and flux-closure. These topological defects can be tuned by varying topological surface geometry and mechanical loading conditions. As studied recently, the exotic topological defects in ferroelectric perovskite materials, like flux-closure domains, skyrmion lattice, and polar meron, present novel properties under mechanical, optical, and electric fields.[12,47] The discovery of similar topological polar structures in 2D materials developed the knowledge of polar skyrmion fields and revealed the potential application of those various tunable topological patterns of 2D FE materials in future high-density storage.[14]

4. Experimental Section

DFT Calculations: The first-principles calculations in this work were performed based on the density-functional theory (DFT), as implemented in the Vienna Ab initio Simulation Package (VASP).[55–58] Projector augments wave pseudopotentials with the Perdew-Burke-Ernzerhof (PBE) exchange-correlation and generalized gradient approximation (GGA) were employed.[59–61] For all calculations, the plane-wave cutoff was set to be 600 eV. A Monkhorst-Pack gamma-centered k-points grid of dimensions 25× 25 ×1 was adopted for the unit cell.[62] The cell height in the direction normal to the surface plane was fixed as 20 Å to avoid the interactions between adjacent layers. In all cases, the atoms were fully relaxed in all directions until the force on each atom was less than 0.001 eVÅ^{-1}, ensuring the accuracy for the optimization of structure. The electric polarization was directly computed via "berry-phase" theory.[37]

Machine Learning Potential: The MD simulation with machine learning potential was performed to get an insight on the atomic picture of the PbTe under strain and finite temperature. The machine learning potential was constructed by the DeepMD packages[63,64] based on the dataset provided by DFT calculations, as demonstrated in the flow chart of Figure S25 (Supporting Information). The configurations under different strain and temperature (10 −− 400 K) were sampled by the short AIMD simulations picked up every ten steps. The whole dataset consists of 100 K different labeled samples. AIMD calculation of PbTe were performed using VASP. The MD simulations had included the flexoelectricity effect by including the structures under various strain gradients in the training set of deep-learning potentials.

In the DeepMD model, the potential energy E of a configuration was assumed to be a sum of each atomic energy E_i of atom i, which was fitting from a descriptor D_i through an embedding network. The descriptor D_i characterizes the local environment of atom i within a cutoff radius R_c. Here, the R_c was set to 7.5 Å. The maximum number of atoms within the R_c was set to 95 for Pb, 95 for Te, respectively. The translational, rotational, and permutational symmetry of the D_i were preserved by an embedding network. The smooth edition of the DeepMD model was employed to remove the discontinuity introduced by the cutoff radius. The inner cutoff where the smooth begins was set to 7.2 Å. The sizes of the embedding and fitting networks were (25, 50, 100) and (240, 240, 240), respectively. The loss function is defined as:

$$L(p_\varepsilon, p_f, p_\xi) = p_\varepsilon \Delta\varepsilon^2 + \frac{p_f}{3N}\sum_i |\Delta F_i|^2 + \frac{p_\xi}{9}\|\Delta\xi^2\| \quad (1)$$

where $\Delta\xi$, ΔF_i, and $\Delta\xi$ represent the energy, force, and virial tensor difference between the DeepMD model prediction and the training dataset (from DFT calculations). The p_ε, p_f, and p_ξ are weight coefficients of energy, force, and virial tensor. The p_ε increase from 0.02 to 1, and p_f decreases from 1000 to 1 during the training procedure. The virial tensor was discarded in this study, thus the p_ξ is set to 0. The DeepMD models were trained for 6 000 000 steps. Subsequently, various tests had been made to testify the accuracy of the machine learning potential.

The obtained machine learning potential performed well at larger scale and could reproduce the phase transition results of DFT calculations, as shown in Figure S26 (Supporting Information). A detailed verification of this potential was elaborated in another work.

MD Simulation: With the well-testified machine learning potential, equilibrium MD simulations were performed using LAMMPS packages in a temperature of 300 K.[65,66] The 60 × 60 2D PbTe supercell (14400 atoms) was used and the duration of the MD simulation was 90 ps with a 1 fs time step. The atomic velocities and positions were collected every 1 ps under the NVT ensemble for the calculation of the offset ($\vec{R}$) of nearest Pb and Te atoms. This offset was taken as the polarization of the 2D PbTe in the specific position and then projected to the XOY plane to give a better visual presentation.

FEM Methods: The unique strain fields of 2D PbTe at macro-scale were designed by FEM simulations. The 2D PbTe was taken as an elastic anisotropic membrane with different elastic constants before and after the phase transition in the simulation. The parameters used in the calculation

are listed in Table S1 (Supporting Information). During the indentation, it was fixed on the matrix by restricting all the degree of freedom around the edges and the indenters and holes with different shapes were adopted. Subsequently, the polarization direction was decided according to polarization-strain diagram obtained by DFT calculations.

Supporting Information

Supporting Information is available from the Wiley Online Library or from the author.

Acknowledgements

The authors gratefully acknowledged the support of NSFC (Grant no.11974269), the support by the Key Research and Development Program of Shaanxi (Grant no. 2023-YBGY-480), and the 111 projects 2.0 (Grant no. BP0618008). J.Z.L. acknowledged the support from ARC discovery projects (Grant no. DP210103888) and HPC from National Computational Infrastructure from Australia. The authors also thank F. Yang and X.D. Zhang at the Network Information Center of Xi'an Jiaotong University for supporting the HPC platform. This work was also supported by State Key Laboratory for Mechanical Behavior of Materials.

Conflict of Interest

The authors declare no conflict of interest.

Author Contributions

B.X., Z.G., and J.L. contributed equally to this work. The manuscript was written through contributions of all authors. All authors have given approval to the final version of the manuscript.

Data Availability Statement

The data that support the findings of this study are available in the supplementary material of this article.

Keywords

2D materials, ferroelectrics, polar topological, skyrmion, strain engineering

Received: September 22, 2023
Revised: January 6, 2024
Published online:

[1] W. Jiang, P. Upadhyaya, W. Zhang, G. Yu, M. B. Jungfleisch, F. Y. Fradin, J. E. Pearson, Y. Tserkovnyak, K. L. Wang, O. Heinonen, S. G. E. te Velthuis, A. Hoffmann, *Science* **2015**, *349*, 283.
[2] Y. J. Wang, Y. P. Feng, Y. L. Zhu, Y. L. Tang, L. X. Yang, M. J. Zou, W. R. Geng, M. J. Han, X. W. Guo, B. Wu, X. L. Ma, *Nat. Mater.* **2020**, *19*, 881.
[3] T. Xu, Y. Ichiki, K. Masuda, Y. Wang, H. Hirakata, T. Shimada, *ACS Nano* **2023**, *17*, 10836.
[4] S. Das, M. R. McCarter, F. Gómez-Ortiz, Y.-L. Tang, Z. Hong, A. Ghosh, P. Shafer, P. García-Fernández, J. Junquera, L. W. Martin, R. Ramesh, *Nano Lett.* **2023**, *23*, 6602.
[5] A. R. Damodaran, J. D. Clarkson, Z. Hong, H. Liu, A. K. Yadav, C. T. Nelson, S.-L. Hsu, M. McCarter, K.-D. Park, V. Kravtsov, A. Farhan, Y. Dong, Z. Cai, H. Zhou, P. Aguado-Puente, P. García-Fernández, J. Íñiguez, J. Junquera, A. Scholl, M. B. Raschke, L.-Q. Chen, D. D. Fong, R. Ramesh, L. W. Martin, *Nat. Mater.* **2017**, *16*, 1003.
[6] A. K. Yadav, C. T. Nelson, S. L. Hsu, Z. Hong, J. D. Clarkson, C. M. Schlepütz, A. R. Damodaran, P. Shafer, E. Arenholz, L. R. Dedon, D. Chen, A. Vishwanath, A. M. Minor, L. Q. Chen, J. F. Scott, L. W. Martin, R. Ramesh, *Nature* **2016**, *530*, 198.
[7] S. Chen, S. Yuan, Z. Hou, Y. Tang, J. Zhang, T. Wang, K. Li, W. Zhao, X. Liu, L. Chen, L. W. Martin, Z. Chen, *Adv. Mater.* **2021**, *33*, 2000857.
[8] S. Das, Y. L. Tang, Z. Hong, M. A. P. Gonçalves, M. R. McCarter, C. Klewe, K. X. Nguyen, F. Gómez-Ortiz, P. Shafer, E. Arenholz, V. A. Stoica, S.-L. Hsu, B. Wang, C. Ophus, J. F. Liu, C. T. Nelson, S. Saremi, B. Prasad, A. B. Mei, D. G. Schlom, J. Íñiguez, P. García-Fernández, D. A. Muller, L. Q. Chen, J. Junquera, L. W. Martin, R. Ramesh, *Nature* **2019**, *568*, 368.
[9] H.-Y. Zhang, X.-J. Song, X.-G. Chen, Z.-X. Zhang, Y.-M. You, Y.-Y. Tang, R.-G. Xiong, *J. Am. Chem. Soc.* **2020**, *142*, 4925.
[10] Y. L. Tang, Y. L. Zhu, X. L. Ma, A. Y. Borisevich, A. N. Morozovska, E. A. Eliseev, W. Y. Wang, Y. J. Wang, Y. B. Xu, Z. D. Zhang, S. J. Pennycook, *Science* **2015**, *348*, 547.
[11] P. Behera, E. Parsonnet, F. Gómez–Ortiz, V. Srikrishna, P. Meisenheimer, S. Susarla, P. Kavle, L. Caretta, Y. Wu, Z. Tian, A. Fernandez, L. W. Martin, S. Das, J. Junquera, Z. Hong, R. Ramesh, *Adv. Mater.* **2023**, *35*, 2208367.
[12] Q. Li, V. A. Stoica, M. Paściak, Y. Zhu, Y. Yuan, T. Yang, M. R. McCarter, S. Das, A. K. Yadav, S. Park, C. Dai, H. J. Lee, Y. Ahn, S. D. Marks, S. Yu, C. Kadlec, T. Sato, M. C. Hoffmann, M. Chollet, M. E. Kozina, S. Nelson, D. Zhu, D. A. Walko, A. M. Lindenberg, P. G. Evans, L.-Q. Chen, R. Ramesh, L. W. Martin, V. Gopalan, J. W. Freeland, et al., *Nature* **2021**, *592*, 376.
[13] I. Luk'yanchuk, V. M. Vinokur, *Nature* **2021**, *592*, 359.
[14] L. Han, C. Addiego, S. Prokhorenko, M. Wang, H. Fu, Y. Nahas, X. Yan, S. Cai, T. Wei, Y. Fang, H. Liu, D. Ji, W. Guo, Z. Gu, Y. Yang, P. Wang, L. Bellaiche, Y. Chen, D. Wu, Y. Nie, X. Pan, *Nature* **2022**, *603*, 63.
[15] Q. Zhang, L. Xie, G. Liu, S. Prokhorenko, Y. Nahas, X. Pan, L. Bellaiche, A. Gruverman, N. Valanoor, *Adv. Mater.* **2017**, *29*, 1702375.
[16] Q. Li, C. T. Nelson, S.-L. Hsu, A. R. Damodaran, L.-L. Li, A. K. Yadav, M. McCarter, L. W. Martin, R. Ramesh, S. V. Kalinin, *Nat. Commun.* **2017**, *8*, 1468.
[17] J. Yin, H. Zong, H. Tao, X. Tao, H. Wu, Y. Zhang, L.-D. Zhao, X. Ding, J. Sun, J. Zhu, J. Wu, S. J. Pennycook, *Nat. Commun.* **2021**, *12*, 3632.
[18] K.-E. Kim, S. Jeong, K. Chu, J. H. Lee, G.-Y. Kim, F. Xue, T. Y. Koo, L.-Q. Chen, S.-Y. Choi, R. Ramesh, C.-H. Yang, *Nat. Commun.* **2018**, *9*, 403.
[19] S. Hsu, M. R. McCarter, C. Dai, Z. Hong, L. Chen, C. T. Nelson, L. W. Martin, R. Ramesh, *Adv. Mater.* **2019**, *31*, 1901014.
[20] Y.-T. Shao, S. Das, Z. Hong, R. Xu, S. Chandrika, F. Gómez-Ortiz, P. García-Fernández, L.-Q. Chen, H. Y. Hwang, J. Junquera, L. W. Martin, R. Ramesh, D. A. Muller, *Nat. Commun.* **2023**, *14*, 1355.
[21] S. Yuan, Z. Chen, S. Prokhorenko, Y. Nahas, L. Bellaiche, C. Liu, B. Xu, L. Chen, S. Das, L. W. Martin, *Phys. Rev. Lett.* **2023**, *130*, 226801.
[22] Z. Guan, H. Hu, X. Shen, P. Xiang, N. Zhong, J. Chu, C. Duan, *Adv. Electron. Mater.* **2020**, *6*, 1900818.
[23] C. Cui, F. Xue, W.-J. Hu, L.-J. Li, *npj 2D Mater. Appl.* **2018**, *2*, 1.
[24] Y. Hong, J. Deng, X. Ding, J. Sun, J. Z. Liu, *J. Phys. Chem. Lett.* **2023**, *14*, 3160.
[25] Y. Yang, H. Zong, J. Sun, X. Ding, *Adv. Mater.* **2021**, *33*, 2103469.
[26] W. Wu, L. Wang, Y. Li, F. Zhang, L. Lin, S. Niu, D. Chenet, X. Zhang, Y. Hao, T. F. Heinz, J. Hone, Z. L. Wang, *Nature* **2014**, *514*, 470.

[27] Z. Zheng, Q. Ma, Z. Bi, S. De La Barrera, M.-H. Liu, N. Mao, Y. Zhang, N. Kiper, K. Watanabe, T. Taniguchi, J. Kong, W. A. Tisdale, R. Ashoori, N. Gedik, L. Fu, S.-Y. Xu, P. Jarillo-Herrero, *Nature* **2020**, *588*, 71.
[28] Z. Dai, L. Liu, Z. Zhang, *Adv. Mater.* **2019**, *31*, 1805417.
[29] S. Deng, A. V. Sumant, V. Berry, *Nano Today* **2018**, *22*, 14.
[30] W. Sun, W. Wang, H. Li, G. Zhang, D. Chen, J. Wang, Z. Cheng, *Nat. Commun.* **2020**, *11*, 5930.
[31] H. Wang, X. Qian, *2D Mater.* **2017**, *4*, 015042.
[32] R. Fei, W. Kang, L. Yang, *Phys. Rev. Lett.* **2016**, *117*, 097601.
[33] K. Chang, J. W. D. Villanova, J. Ji, S. Das, F. Küster, S. Barraza–Lopez, P. Sessi, S. S. P. Parkin, *Adv. Mater.* **2021**, *33*, 2102267.
[34] M. P. Jiang, M. Trigo, I. Savic, S. Fahy, E. D. Murray, C. Bray, J. Clark, T. Henighan, M. Kozina, M. Chollet, J. M. Glownia, M. C. Hoffmann, D. Zhu, O. Delaire, A. F. May, B. C. Sales, A. M. Lindenberg, P. Zalden, T. Sato, R. Merlin, D. A. Reis, *Nat. Commun.* **2016**, *7*, 12291.
[35] Y. Zhang, X. Ke, P. R. C. Kent, J. Yang, C. Chen, *Phys. Rev. Lett.* **2011**, *107*, 175503.
[36] P. Chudzinski, *Phys. Rev. Res.* **2020**, *2*, 012048.
[37] R. D. King-Smith, D. Vanderbilt, *Phys. Rev. B* **1993**, *47*, 1651.
[38] R. Resta, *Rev. Mod. Phys.* **1994**, *66*, 899.
[39] R. Fei, W. Li, J. Li, L. Yang, *Appl. Phys. Lett.* **2015**, *107*, 173104.
[40] C. Di Giorgio, E. Blundo, G. Pettinari, M. Felici, F. Bobba, A. Polimeni, *Adv. Mater. Interfaces* **2022**, *9*, 2102220.
[41] T. Xu, X. Wang, J. Mai, J. Zhang, J. Wang, T. Zhang, *Adv. Electron. Mater.* **2020**, *6*, 1900932.
[42] X. Zhang, Z. Yang, Y. Chen, *J. Appl. Phys.* **2017**, *122*, 064101.
[43] G. Lu, S. Li, X. Ding, J. Sun, E. K. H. Salje, *J. Appl. Phys.* **2021**, *129*, 084104.
[44] Z. Guan, Y.-K. Li, Y.-F. Zhao, Y. Peng, G. Han, N. Zhong, P.-H. Xiang, J.-H. Chu, C.-G. Duan, *Nano Lett.* **2022**, *22*, 4792.
[45] T. M. Linker, K.-i. Nomura, S. Fukushima, R. K. Kalia, A. Krishnamoorthy, A. Nakano, K. Shimamura, F. Shimojo, P. Vashishta, *Nano Lett.* **2023**, *23*, 7456.
[46] W.-R. Geng, X. Guo, H.-L. Ge, Y.-L. Tang, Y. Zhu, Y. Wang, B. Wu, M.-J. Zou, Y.-P. Feng, X.-L. Ma, *Nano Lett.* **2022**, *22*, 8892.
[47] Y. L. Tang, *J. Appl. Phys.* **2021**, *129*, 200904.
[48] L. Zhou, C. Dai, P. Meisenheimer, S. Das, Y. Wu, F. Gómez-Ortiz, P. García-Fernández, Y. Huang, J. Junquera, L. Chen, R. Ramesh, Z. Hong, *Adv. Funct. Mater.* **2022**, *32*, 2111392.
[49] Q. Zhang, S. Prokhorenko, Y. Nahas, L. Xie, L. Bellaiche, A. Gruverman, N. Valanoor, *Adv. Funct. Mater.* **2019**, *29*, 1808573.
[50] Y. Zheng, W. J. Chen, *Rep. Prog. Phys.* **2017**, *80*, 086501.
[51] Z. Zhao, X. Ding, E. K. H. Salje, *Appl. Phys. Lett.* **2014**, *105*, 112906.
[52] L. L. Ma, W. J. Chen, B. Wang, W. M. Xiong, Y. Zheng, *J. Phys.: Condens. Matter* **2020**, *32*, 035402.
[53] R. M. Murphy, E. D. Murray, S. Fahy, I. Savic, *Phys. Rev. B* **2016**, *93*, 104304.
[54] T. Xu, J. Zhang, Y. Zhu, J. Wang, T. Shimada, T. Kitamura, T.-Y. Zhang, *Nanoscale Horiz.* **2020**, *5*, 1400.
[55] P. Hohenberg, W. Kohn, *Phys. Rev.* **1964**, *136*, B864.
[56] W. Kohn, L. J. Sham, *Phys. Rev.* **1965**, *140*, A1133.
[57] G. Kresse, J. Hafner, *Phys. Rev. B* **1993**, *47*, 558.
[58] G. Kresse, J. Furthmüller, *Comput. Mater. Sci.* **1996**, *6*, 15.
[59] A. D. Becke, *Phys. Rev. A* **1988**, *38*, 3098.
[60] D. C. Langreth, M. J. Mehl, *Phys. Rev. B* **1983**, *28*, 1809.
[61] J. P. Perdew, K. Burke, M. Ernzerhof, *Phys. Rev. Lett.* **1996**, *77*, 3865.
[62] H. J. Monkhorst, J. D. Pack, *Phys. Rev. B* **1976**, *13*, 5188.
[63] H. Wang, L. Zhang, J. Han, W. E, *Comput. Phys. Commun.* **2018**, *228*, 178.
[64] J. Zeng, D. Zhang, D. Lu, P. Mo, Z. Li, Y. Chen, M. Rynik, L. Huang, Z. Li, S. Shi, Y. Wang, H. Ye, P. Tuo, J. Yang, Y. Ding, Y. Li, D. Tisi, Q. Zeng, H. Bao, Y. Xia, J. Huang, K. Muraoka, Y. Wang, J. Chang, F. Yuan, S. L. Bore, C. Cai, Y. Lin, B. Wang, J. Xu, et al., *J. Chem. Phys.* **2023**, *159*, 054801.
[65] S. Plimpton, *J. Comput. Phys.* **1995**, *117*, 1.
[66] A. P. Thompson, H. M. Aktulga, R. Berger, D. S. Bolintineanu, W. M. Brown, P. S. Crozier, P. J. In 'T Veld, A. Kohlmeyer, S. G. Moore, T. D. Nguyen, R. Shan, M. J. Stevens, J. Tranchida, C. Trott, S. J. Plimpton, *Comput. Phys. Commun.* **2022**, *271*, 108171.